ACS Energy LETTERS

http://pubs.acs.org/journal/aelccp

LETTER

Modeling and Simulation of the Spatial and Light-Intensity Dependence of Product Distributions in an Integrated Photoelectrochemical CO_2 Reduction System

Yikai Chen, Nathan S. Lewis,* and Chengxiang Xiang*

Division of Chemistry and Chemical Engineering, California Institute of Technology, Pasadena, California 91125, United States

ABSTRACT: **A multiphysics model that accounts for the performance of electrocatalysts and triple-junction light absorbers, as well as for the transport properties of the electrolyte and dissolved CO_2, was used to evaluate the spatial and light-intensity dependence of product distributions in an integrated photoelectrochemical CO_2 reduction (CO_2R) cell. Different sets of band gap combinations of triple-junction light absorbers were required to accommodate the optimal total operating current density relative to the optimal partial current density for CO_2R. The simulated product distribution was highly nonuniform along the width of the electrode and depended on the electrode dimensions as well as the illumination intensity. To achieve the same product selectivity as in a potentiostatic, "half-cell" configuration, the electrocatalyst must retain its selectivity over a range of cathode potentials, and this range is dependent on the transport losses and current−voltage relationship of the light absorbers, the geometric parameters of the cell, and the illumination intensity.**

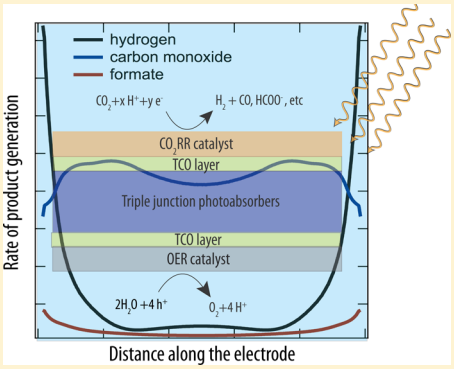

An efficient solar-driven CO_2 reduction system[1−5] requires effective delivery of CO_2 to the electrode surface, selective reduction of CO_2 by an active electrocatalyst at the cathode, adequate ionic transport between the anolyte and catholyte chambers, and robust and cost-effective methods for separating the products. Electrocatalysts including metals,[6,7] metal alloys,[8] metal oxides,[9] and semiconductors[10−14,10,15] have been investigated for electrocatalytic CO_2 reduction (CO_2R). For most electrocatalysts operated in contact with aqueous electrolytes, the branching ratio between water reduction (i.e., the hydrogen-evolution reaction, HER) and CO_2R depends on the applied potential.[9] For instance, in a three-electrode potentiostatic configuration, the Faradaic efficiency for the production of formate, $HCOO^-$, at the surface of an oxidized Cu foil changes from 5.5% to 32.9% when the potential of the working electrode is changed by ∼20 mV.[9] In contrast to experiments performed using three-electrode potentiostatic configurations, the potential at the cathode of a full photoelectrosynthetic cell depends on the reaction kinetics at the anode surface as well as transport losses associated with solution resistance, electrodialysis, pH gradients, and CO_2 concentration gradients near the surface of the cathode. Modeling and simulation has shown that many test-bed configurations for water-splitting devices produce spatially dependent potential distributions, with variations of >100 mV across the electrode surface even under constant illumination intensity.[16−19] Moreover, variation in the illumination intensity during operation additionally affects the solar-to-fuel (STF) conversion efficiency for such systems.

Herein, a two-dimensional numerical model has been developed using COMSOL Multiphysics to evaluate the spatial and temporal variation of the product distribution in an integrated photoelectrochemical CO_2 reduction cell driven by triple-junction light absorbers operating at the Shockley−Queisser (S-Q) limit. The current−voltage behaviors and the Faradaic efficiencies of metallic Cu and Ag catalysts, respectively, for CO_2R in 0.10 M bicarbonate solution (pH 6.8)[8,20] were used to describe the reactions at the cathode. For the metallic Ag catalyst, the following CO_2R reactions were included at the electrode surface:

$$2H^+ + 2e^- \rightarrow H_2$$

$$CO_2 + 2H^+ + 2e^- \rightarrow HCOOH$$

$$CO_2 + 2H^+ + 2e^- \rightarrow CO + H_2O$$

For the metallic Cu catalyst, two additional CO_2R reactions were included at the electrode surface:

Received: May 10, 2016
Accepted: June 8, 2016

DOI: 10.1021/acsenergylett.6b00134
ACS Energy Lett. 2016, 1, 273−280

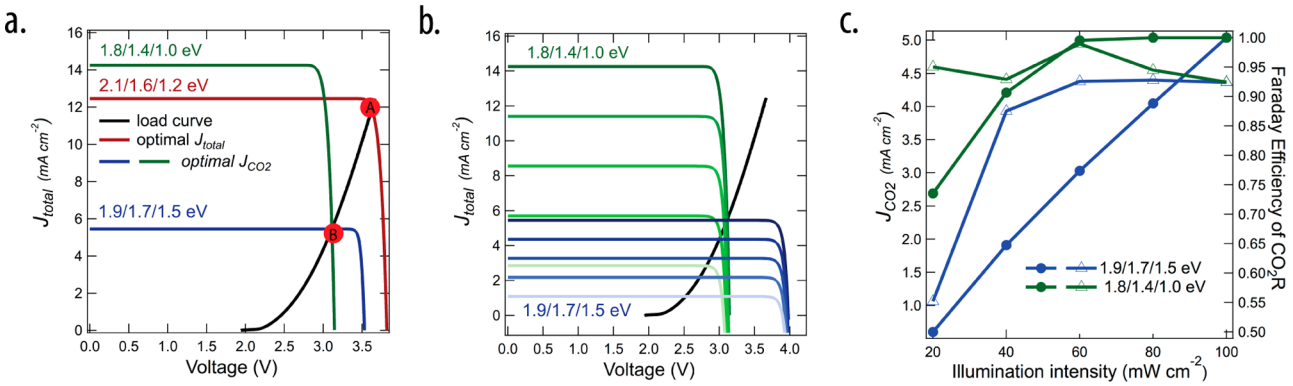

Figure 1. (a) Calculation of the optimal J_{total} (point A) from the crossing point determined by the overall load-curve (black) and the power curve (red) from a triple-junction light-absorber device with an optimal band-gap combination of 2.1 eV/1.6 eV/1.2 eV (device 1) and the calculation of the optimal J_{CO_2} (point B) from the crossing point determined by the overall load curve and two power curves from triple-junction light-absorber devices having optimal band-gap combinations of 1.9 eV/1.7 eV/1.5 eV (blue, device 2) and 1.8 eV/1.4 eV/1.0 eV (green, device 3) in a one-dimensional cell configuration. (b) Overall load curve for CO_2R and OER and the current−voltage characteristics of two ideal triple-junction light absorbers (devices 2 and 3) under different illumination intensities. (c) J_{CO_2} (solid circles, left axis) and the Faradaic efficiency of CO_2R (hollow triangles, right axis) as a function of the illumination intensity for two different triple-junction light absorbers (devices 2 and 3) that produced the same J_{CO_2} and J_{total} at a simulated light intensity of 100 mW cm^{-2} of air mass (AM) 1.5 global illumination.

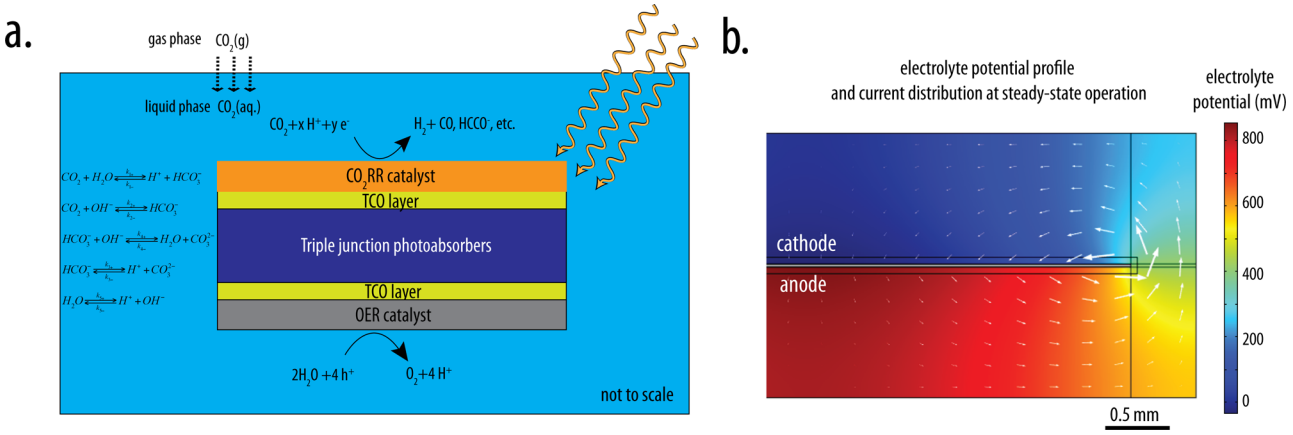

Figure 2. (a) Schematic illustration of an integrated PEC CO_2 reduction cell. (b) Snapshot of the electrolyte potential profile and current distribution (white arrows) of an integrated photoelectrochemical CO_2 reduction cell under steady-state operation. The potential at the middle of the cathode was set to 0 V. The size of the arrow indicates the magnitude of the ionic current density.

$$CO_2 + 8H^+ + 8e^- \rightarrow CH_4 + 2H_2O$$

$$2CO_2 + 12H^+ + 12e^- \rightarrow C_2H_4 + 4H_2O$$

Because of the lack of experimental data for OER catalysts at pH 6.8 or in contact with bicarbonate solutions, the current−voltage behavior of a phosphate-containing CoO_x, Co-Pi, in 0.10 M K-Pi (aq) solution at pH 7.2[21] was used to describe the reactions at the anode. No membrane was included in the model, and any transport loss produced by a membrane separator was neglected. The model also assumed robust separation of products by neglecting reactions such as oxidation of the reduced products at the anode, reduction of O_2 at the cathode, or recombination of products in the solution.

Figure 1a shows the current−voltage characteristics of three triple-junction light-absorber devices that are operating at the Shockley−Queisser limit, as well as the overall load curve for Ag performing the CO_2R reaction and Co-Pi performing the OER in a one-dimensional, face-to-face cell design. The operational current density of the overall reaction, J_{total}, was determined by the crossing point between the load curve (black) and the power curve (green, blue, or red) of the light-absorber device. The optimal J_{total} of 11.9 mA cm^{-2} was obtained at the maximum power point of the red curve (point A), which corresponded to a band-gap combination of 2.1, 1.6, and 1.2 eV for the top band gap, middle band gap, and bottom band gap, respectively, of the light-absorber structure (device 1). However, the cathode overpotential at the optimal J_{total} was 1.4 V, which led to a Faradaic efficiency of 36% for all CO_2R products (CO and HCO_3^-) and a Faradaic efficiency of 64% for H_2. The partial current density that corresponded to CO_2R, J_{CO_2}, was thus low (4.3 mA cm^{-2}).

In contrast, the blue and green power curves, which correspond to band-gap combinations of 1.9 eV/1.7 eV/1.5 eV (device 2) and 1.8 eV/1.4 eV/1.0 eV (device 3), respectively, yielded an optimal J_{CO_2} of 5.0 mA cm^{-2}, even though J_{total} (point B) (5.5 mA cm^{-2}) was lower than its value at point A (11.9 mA cm^{-2}). A series of band-gap combinations that produced the crossing point at point B would thus yield

DOI: 10.1021/acsenergylett.6b00134
ACS Energy Lett. 2016, 1, 273−280

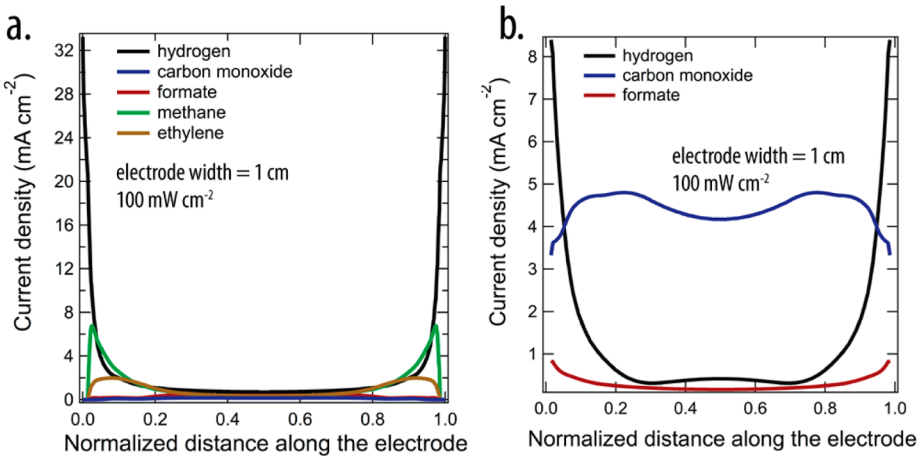

Figure 3. Product distribution for the CO_2R reaction as a function of the normalized distance along 1 cm electrodes for the Cu catalyst (a) and the Ag catalyst (b) in an integrated photoelectrochemical CO_2 reduction cell that incorporates the optimal triple-junction (2.1 eV/1.6 eV/1.1 eV for the Cu catalyst and 2.1 eV/1.6 eV/1.2 eV for the Ag catalyst) light-absorber structure under 100 mW cm^{-2} of simulated AM 1.5 G illumination.

the optimal J_{CO_2} for this specific catalyst system and cell architecture.

Figure 1b depicts the dependence of the current−voltage characteristics of device 2 and device 3 on the light intensity. The two light-absorber structures yielded identical J_{total} and J_{CO_2} values under 100 mW cm^{-2} of simulated air mass (AM) 1.5 G illumination. However, when the illumination intensity was decreased from 100 mW cm^{-2} to 20 mW cm^{-2}, device 2 exhibited a shift in the total operational voltage, from 3.1 to 2.5 V, larger than that of device 3. Figure 1c shows the light-intensity dependence for devices 2 and 3 of the Faradaic efficiency for CO_2R. The Faradaic efficiency for CO_2R for device 2 (blue triangles, right axis) varied from 93% to 55% as the light intensity varied from 100 to 20 mW cm^{-2}, whereas the Faradaic efficiency for CO_2R for device 3 (green triangles, right axis) remained nearly constant (93% to 95%) over the same range of illumination intensities. The J_{CO_2} of device 2 (blue circles, left axis) exhibited a linear dependence on the illumination intensity, because the crossing points between the load curve and the photodiode characteristic occurred in the plateau region of the photodiode curve. In contrast, J_{CO_2} of device 3 (green circles, left axis) exhibited a weaker dependence on the illumination intensity, because the crossing points occurred at the rising portion of the photodiode curve. Hence, even in a one-dimensional cell architecture as shown in Figure 1, the rate of formation of CO_2R products, as well as the ratio of CO_2R products to hydrogen, varied as the illumination intensity changed and were dependent on the choice of the light absorbers. The different product branching ratio under varying illumination conditions that result from the diurnal cycle as well as siting of a deployed system will thus have an impact on product mixtures as well as on requirements for product separation and collection processes in solar-driven CO_2R devices.

Figure 2a shows a schematic illustration of an integrated, two-dimensional photoelectrosynthetic CO_2 reduction cell in which the triple-junction light absorber (blue) is coated on the top by a transparent conductive oxide (TCO) layer and a CO_2R catalyst, and on the bottom by a TCO layer and an OER catalyst. The thickness of the TCO layer was set to 10 μm, and the conductivity of the TCO was set to 10^5 S m^{-1}. In this cell, a bicarbonate solution that contained 0.1 M $NaHCO_3$(aq) was equilibrated with 1 atm pressure of CO_2(g). The concentration of CO_2 in the aqueous solution was set to 34 mM, according to Henry's law. The detailed cell dimensions are summarized in Computational Methods. Figure 2b shows a snapshot of the electrolyte potential profile and the associated current distribution in the PEC cell. The potential profile of the electrolyte was determined by iteratively solving the equations that describe in a two-dimensional simulation domain the current−voltage relationship of the light absorber, transport losses in the electrolyte, and the electrocatalytic performance of the catalysts. Generally, a larger transport loss would result in a larger difference in the electrolyte potentials for the cathode and anode regions, and would result in a smaller kinetic overpotential as well as a smaller operational current density at the electrode surface. As shown in Figure 2b, the operating current densities for the OER and CO_2R were concentrated at the edge of the device because of the short ionic path length and the low solution resistive losses at such positions relative to other positions on the device. The CO_2R current density at the edge of the electrode was ~4.5 times larger than the CO_2R current density at the middle of the electrode. Moreover, when the electrode width was 1.0 cm, the potential at the cathode varied spatially by >400 mV.

Figure 3 shows the distribution of products from water reduction and CO_2R, as well as the partial current density for each of the major products, as a function of the normalized distance along the electrode, for the Cu catalyst (Figure 3a) and for the Ag catalyst (Figure 3b) in an integrated PEC CO_2 reduction cell under 100 mW cm^{-2} of simulated AM 1.5 G illumination. The normalized distance along the electrode was a unitless parameter that was defined as the distance from one end of the electrode normalized to the width of the electrode. Because a series of band-gap combinations would yield the same J_{CO_2}, the band-gap combinations that produced the optimum J_{total} were used for the Cu catalyst (2.1 eV/1.6 eV/1.1 eV) and the Ag catalyst (2.1 eV/1.6 eV/1.2 eV) to permit evaluation of the resulting spatial distribution of the reduction products under such conditions. The mathematical forms of the transport losses modeled for the two-dimensional PEC cell are described in Computational Methods and include the resistive loss and electrodialysis of the electrolyte, as well as the

DOI: 10.1021/acsenergylett.6b00134
ACS Energy Lett. 2016, 1, 273−280

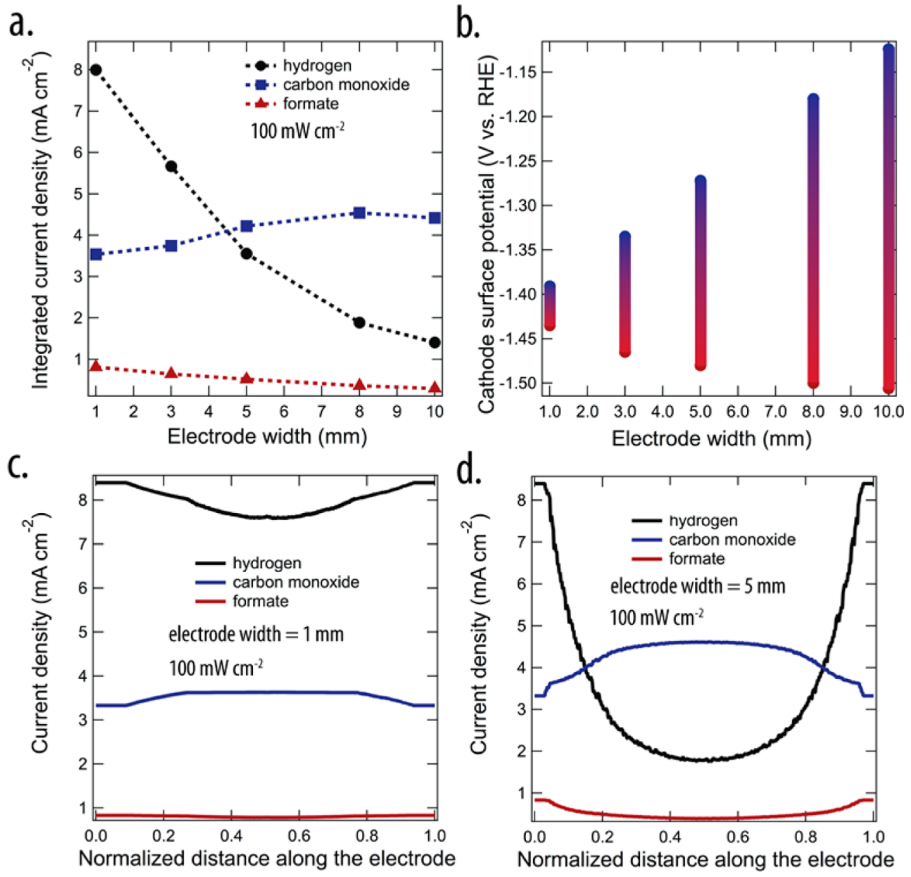

Figure 4. (a) Integrated CO_2R product distribution as a function of the electrode width for the Ag catalyst in the integrated PEC CO_2 reduction cell that incorporates the optimal triple-junction light-absorber structure (device 1, 2.1 eV/1.6 eV/1.2 eV) under simulated 100 mW cm^{-2} of AM 1.5 G illumination. (b) Cathode surface potential and its variation as a function of the electrode width under 100 mW cm^{-2} of simulated AM 1.5 G illumination. (c) Partial current density for hydrogen, carbon monoxide, and formate as a function of the normalized distance along the electrode when the electrode width of the cell was set to (c) 1.0 mm and (d) 5.0 mm.

concentration overpotentials associated with pH gradients and CO_2 concentration gradients at the electrode surface. Moderate agitation and convection of the electrolyte was assumed by taking the thickness of the hydrodynamic boundary layer to be 100 μm. Consequently, under 100 mW cm^{-2} illumination, the voltage losses due to pH gradients, CO_2 concentration gradients, and electrodialysis of the electrolyte were <100 mV for the largest electrode width. The resistive loss in the bicarbonate solution comprised the largest component of the transport loss in the system. Because no membrane was included and moderate convection (boundary layer thickness = 100 μm) was introduced in the model, small voltage losses due to the pH gradients and electrodialysis were obtained in the calculation relative to the losses that are present and have been evaluated quantitatively for near-neutral pH systems for water-splitting reactions.[22,23]

For the Cu catalyst, H_2 was the dominant (nearly 100 mol % of the total) product near the edge of the electrode because of the small solution transport losses, high overpotential for the CO_2R, and high Faradaic efficiency for hydrogen evolution at such potentials. In contrast, at the midpoint of the electrode, ~52% of the current led to H_2(g). Similar variations of the product distributions were observed when Ag was the CO_2R electrocatalyst. Thus, the spatial variation of the product distributions as shown in Figure 3, and the resulting overall product branching ratio in full electrochemical devices, could be very different from the Faradaic efficiency for production of various products determined by three-electrode measurements under well-controlled potentials with equipotential electrode surfaces. Numerical modeling of photoreactors that have realistic dimensions, under realistic operating conditions, therefore is needed to obtain a firm prediction of the performance of the whole cell by using the intrinsic materials properties of the system in conjunction with the transport properties of the reactant, product, and reaction media.

Figure 4a shows the integrated current densities over the electrode width for H_2 (black), CO (blue), and formate (red), as a function of the width of the electrode, in a cell with Ag as the CO_2R catalyst. As the electrode width increased from 1.0 mm to 1.0 cm, the integrated partial current density for H_2 (black) decreased from 8 mA cm^{-2} to 1.4 mA cm^{-2}, and the integrated partial current density for CO (blue) increased slightly, from 3.5 mA cm^{-2} to 4.4 mA cm^{-2}. The reduction in transport losses as the electrode width decreased resulted in the change in the integrated current densities as well as in the spatial variation of the product distribution.

Figure 4b shows the dependence of the potential at the surface of the cathode on the width of the electrode, under 100 mW cm^{-2} of simulated AM 1.5 G illumination. The surface potential at any particular location on the cathode was determined by the overall transport losses (solution resistive loss, electrodialysis of electrolyte, and voltage losses associated with pH gradients and CO_2 concentration gradients), the current−voltage characteristics of the light absorbers, the

DOI: 10.1021/acsenergylett.6b00134
ACS Energy Lett. 2016, 1, 273−280

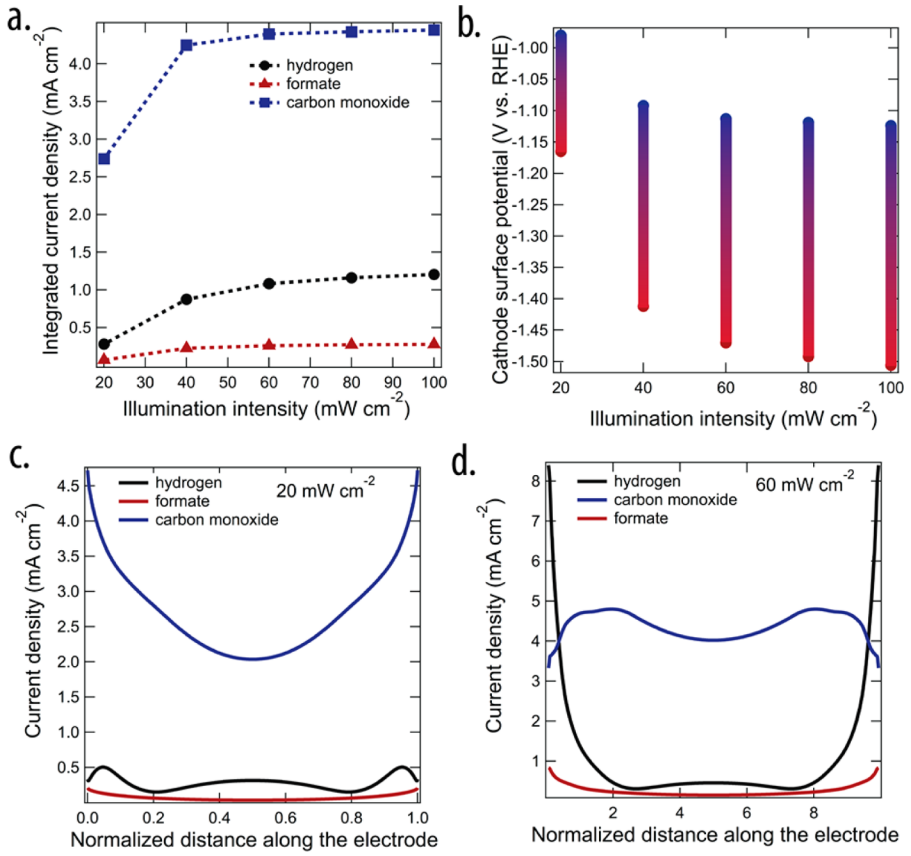

Figure 5. (a) Integrated CO_2R reaction product distribution as a function of the illumination intensity for the Ag catalyst in the integrated PEC CO_2 reduction cell that incorporates the optimal triple-junction light-absorber structure (2.1 eV/1.6 eV/1.2 eV). (b) Cathode surface potential and its variation as a function of the illumination intensity. The partial current density for hydrogen, carbon monoxide, and formate as a function of the normalized distance along the electrode under (c) 20 mW cm^{-2} illumination and (d) 60 mW cm^{-2} of simulated AM 1.5 G illumination. The electrode width was set to 1.0 cm for all calculations in this figure.

behavior of the OER catalyst, and the lateral conduction properties of the TCO layers. The spatial variation in the potential of the cathode produced a variable product distribution along the width of the electrode. Panels c and d of Figure 4 show the partial current density as a function of the normalized distance along the electrode when the electrode width was set to 1.0 mm and 5.0 mm, respectively. Under constant illumination (100 mW cm^{-2}), the cathode surface potential varied by >400 mV when the electrode width was 1.0 cm, but the cathode surface potential varied by <50 mV when the electrode width was decreased to 1.0 mm. The greater variation in surface potential for the larger electrode resulted in a greater variation in the product distribution along the surface of the larger electrode than the smaller electrode; thus, the two electrodes would yield different product distributions: the 1 mm electrode yields 65% H_2, 28% CO, and 7% formate, while the 5 mm electrode yields 43% H_2, 51% CO, and 6% formate. To achieve the same level of selectivity as in a potentiostatically controlled, "half-cell" configuration, nearly constant Faradaic efficiencies for the products are required across the operating voltage windows (indicated by the gradient bars in Figure 4b). As the electrode dimension increased, the voltage window of required constant Faradaic efficiency also increased. Note that the selectivity of the CO_2R catalyst in this study was defined as maintaining the ratios of Faradaic efficiencies among all of the various reduced products in the system. Depending on the end-use of the reduced products, a mixture of carbon-containing products, including products in liquid or gaseous phases or both, could be valuable. The model described herein can be used to design the cell geometry to produce the desired product branching ratios in a realistic PEC cell under various illumination conditions.

Figure 5a shows the integrated current densities over the electrode width for H_2 (black), CO (blue), and formate (red) as a function of the illumination intensity, with Ag as the CO_2R catalyst. The integrated partial current density for all of the products increased as the illumination intensity increased. However, the partial current density did not scale linearly with the illumination intensity. The product distribution also varied because of the nonmonotonic product distribution produced by the Ag catalyst as a function of potential. Figure 5b shows the cathode surface potential and its variation as a function of the illumination intensity, when the electrode width was set to 1.0 cm. Furthermore, panels c and d of Figure 5 show the detailed partial current density of H_2 (black), CO (blue), and formate (red) as a function of the normalized distance along the electrode under 20 and 60 mW cm^{-2}, respectively, of simulated AM 1.5 G illumination. For an integrated PEC cell having this specific design, with an electrode width of 1.0 cm under varying illumination intensities, achieving the same product selectivity as in a potentiostatically controlled three-electrode, "half-cell" configuration would require a constant CO_2R Faradaic efficiency for potentials in the range between 0.98 and 1.50 V versus the reversible hydrogen electrode (RHE).

DOI: 10.1021/acsenergylett.6b00134
ACS Energy Lett. 2016, 1, 273−280

In summary, integrated photoelectrosynthetic CO_2R cells will require a different triple-junction light absorber to optimize J_{CO_2} than the light-absorber structure that optimizes J_{total}. The partial current densities for each of the reduction products will depend on the electrode dimensions and on the illumination intensity. The surface potential variation in a realistic cell under varying light intensities, relative to a potentiostaticallly controlled, "half-cell" configuration, would require catalysts with a substantial voltage window within which the Faradaic efficiency for each product remains unchanged. For example, a cathode voltage window of ~400 mV with constant Faradaic efficiency for each product is required for an integrated PEC architecture with an electrode width of 1.0 cm under varying illumination conditions.

COMPUTATIONAL METHODS

The coupled equations under the corresponding boundary conditions for the one-dimensional and two-dimensional cell architectures were solved using a commercial finite-element program, COMSOL Multiphysics. In the one-dimensional cell architecture, the cathode and anode were arranged face-to-face and were separated by 4 mm. In the two-dimensional cell architecture (Figure 2a), the ratio between the width of the photoelectrodes and the width of the entire unit cell was set to 0.9. The electrolyte height above the cathode surface and below the anode surface was set to 5 mm. A hydrodynamic boundary layer with a thickness of 100 μm was used to account for moderate convection near the photoelectrode. To account for the convective forces in the cell, effective diffusion coefficients for solution species were used beyond the hydrodynamic boundary layer in the bulk solution.

The current−voltage behavior of the triple-junction light-absorber device was obtained from the Shockley−Queisser model and was subsequently fitted using the ideal diode relationship:

$$J = J_{ph} - J_0\left\{\exp\left[\frac{q(V + JR_s)}{kT}\right] - 1\right\} \tag{1}$$

The transport of electrons and holes within the TCO layer was described using Ohm's Law:

$$j_s = -\sigma_s \nabla \phi_s \tag{2}$$

where j_s represents the current density; σ_s is the electrical conductivity of the TCO layer, and $\nabla\phi_s$ is the electric potential gradient within the TCO layer.

The current density versus potential characteristics and the Faradaic efficiency of the metallic Cu and Ag catalysts for CO_2R were based on experimental data[8,20] and were fitted into piecewise functions, in which the subfunctions were described by the Butler−Volmer relation:

$$J_{OER/CO_2RR} = J_{0,OER/CO_2RR}\left[\exp\left(\frac{\alpha_{a,OER/CO_2RR} F\eta}{RT}\right) - \exp\left(-\frac{\alpha_{c,OER/CO_2RR} F\eta}{RT}\right)\right] \tag{3}$$

where $J_{0,OER/CO_2RR}$ is the exchange-current density for the OER or CO_2R reaction, respectively and $\alpha_{a,OER/CO_2RR}$ and $\alpha_{c,OER/CO_2RR}$ are the anodic and cathodic transfer coefficients, respectively, for the OER or the CO_2R reaction. The overpotential, η, is defined as

$$\eta = \phi_s - \phi_l - \phi_0 \tag{4}$$

where ϕ_s and ϕ_l are the corresponding electric and electrolyte potential at the electrode−electrolyte interface and ϕ_0 is the equilibrium potential. The solution transport that includes diffusion, migration, convection, and bulk reactions of water or buffer dissociation was given by the Nernst−Plank equation. Ionic species, including protons, hydroxide, bicarbonate, carbonate, and potassium ions, as well as neutral species including water, dissolved CO_2, and carbonic acid, were included in the model. The net flux of species in the electrolyte can be written as the sum of fluxes due to migration, diffusion, and convection

$$\mathbf{N}_i = \underbrace{-D_i \nabla c_i}_{\text{Diffusion}} \underbrace{- z_i u_i F c_i \nabla \phi_l}_{\text{Migration}} \underbrace{+ \mathbf{v} c_i}_{\text{Convection}} \tag{5}$$

where ϕ_l is the electric potential, $\mathbf{v}$ the velocity, c_i the concentration, D_i the diffusion coefficient, z_i the charge number, u_i the mobility of ions, and $\mathbf{N}_i$ the molar flux of the ith species. The convection term in the simulation was approximated by a hydrodynamic boundary layer with a thickness of 100 μm.

The transport loss, $\Delta\phi_{transport}$, in the system includes the solution losses, $\Delta\phi_{solution}$; the voltage losses associated with pH gradients, $\Delta\phi_{pHgradient}$; and CO_2 concentration gradients at the electrode surface, $\Delta\phi_{CO_2gradient}$. The transport loss was given by

$$\Delta\phi_{transport} = \Delta\phi_{solution} + \Delta\phi_{pHgradient} + \Delta\phi_{CO_2gradient} \tag{6}$$

The solution loss, $\Delta\phi_{solution}$, was given by

$$\Delta\phi_{solution} = \int \frac{J}{\kappa} dx + \sum_i \int \frac{F z_i D_i \nabla c_i}{\kappa} dx \tag{7}$$

where the first term represents the ohmic resistive loss and the second term represents the electrodialysis loss; ϕ is the electric potential, κ the conductivity of the electrolyte, J the current density, x the distance along the axis of the one-dimensional model, F Faraday's constant, z the charge number, D_i the diffusion coefficient, c_i the molar concentration of the ith species, R the gas constant, and T the absolute temperature.

The Nernstian potential losses associated with the pH gradients, $\Delta\phi_{pHgradient}$, and CO_2 concentration gradients, $\Delta\phi_{CO_2gradient}$, at the surface of the electrodes can be expressed as

$$\Delta\phi_{pHgradient} = 2.303\frac{RT}{F}(pH_{cathode} - pH_{anode})$$
$$\Delta\phi_{CO_2gradient} = \frac{59(mV)}{n}\log\left(\frac{p_{CO_2,cathode}}{p_{CO_2,bulk}}\right) \tag{8}$$

n is the number of electrons transferred in the CO_2 reduction process; for example, n = 2 for CO_2 to formate and n = 8 for CO_2 to methane. $p_{CO_2,cathode}$ and $p_{CO_2,bulk}$ are the partial pressures of CO_2 at the cathode surface and in the bulk solution, respectively.

The chemical reactions included in the bicarbonate solution in this study were

$$CO_2 + H_2O \underset{k_{1-}}{\overset{k_{1+}}{\rightleftarrows}} H^+ + HCO_3^- \tag{9}$$

DOI: 10.1021/acsenergylett.6b00134
ACS Energy Lett. 2016, 1, 273−280

$$CO_2 + OH^- \underset{k_{2-}}{\overset{k_{2+}}{\rightleftarrows}} HCO_3^- \quad (10)$$

$$HCO_3^- \underset{k_{3-}}{\overset{k_{3+}}{\rightleftarrows}} H^+ + CO_3^{2-} \quad (11)$$

$$HCO_3^- + OH^- \underset{k_{4-}}{\overset{k_{4+}}{\rightleftarrows}} H_2O + CO_3^{2-} \quad (12)$$

$$H_2O \underset{k_{5-}}{\overset{k_{5+}}{\rightleftarrows}} H^+ + OH^- \quad (13)$$

where k_{1+}, k_{2+}, k_{3+}, k_{4+}, and k_{5+} are the forward rate constants and k_{1-}, k_{2-}, k_{3-}, k_{4-}, and k_{5-} are the reverse rate constants, respectively, for each reaction. Table 1 summarizes the rate constants and diffusion coefficients of solution species in the simulation.[24−26]

Table 1. Rate Constants and Diffusion Coefficients of Solution Species in the Simulation[24−26]

$CO_2 + H_2O \underset{k_{1-}}{\overset{k_{1+}}{\rightleftarrows}} H^+ + HCO_3^-$	$k_{1+} = 0.037\ s^{-1}$
	$k_{1-} = 7.83 \times 10^4\ M^{-1}\ s^{-1}$
$CO_2 + OH^- \underset{k_{2-}}{\overset{k_{2+}}{\rightleftarrows}} HCO_3^-$	$k_{2+} = 2.23 \times 10^3\ M^{-1}\ s^{-1}$
	$k_{2-} = 4.85 \times 10^{-5}\ s^{-1}$
$HCO_3^- \underset{k_{3-}}{\overset{k_{3+}}{\rightleftarrows}} H^+ + CO_3^{2-}$	$k_{3+} = 2.5\ s^{-1}$
	$k_{3-} = 5 \times 10^{-10}\ M^{-1}\ s^{-1}$
$HCO_3^- + OH^- \underset{k_{4-}}{\overset{k_{4+}}{\rightleftarrows}} H_2O + CO_3^{2-}$	$k_{4+} = 6 \times 10^9\ M^{-1}\ s^{-1}$
	$k_{4-} = 1.2\ s^{-1}$
D_{H^+}	$1.9 \times 10^{-5}\ cm^2\ s^{-1}$
D_{OH^-}	$9.3 \times 10^{-5}\ cm^2\ s^{-1}$
$D_{HCO_3^-}$	$1.2 \times 10^{-5}\ cm^2\ s^{-1}$
$D_{CO_3^{2-}}$	$0.9 \times 10^{-5}\ cm^2\ s^{-1}$
D_{CO_2}	$1.9 \times 10^{-5}\ cm^2\ s^{-1}$

AUTHOR INFORMATION

Corresponding Authors

*E-mail: nslewis@caltech.edu.

*E-mail: cxx@caltech.edu.

Notes

The authors declare no competing financial interest.

ACKNOWLEDGMENTS

This material is based upon work performed by the Joint Center for Artificial Photosynthesis, a DOE Energy Innovation Hub, supported through the Office of Science of the U.S. Department of Energy under Award Number DE-SC0004993.

REFERENCES

(1) Sato, S.; Arai, T.; Morikawa, T. Toward solar-driven photocatalytic CO_2 reduction using water as an electron donor. *Inorg. Chem.* **2015**, *54*, 5105−5113.

(2) Schreier, M.; Curvat, L.; Giordano, F.; Steier, L.; Abate, A.; Zakeeruddin, S. M.; Luo, J. S.; Mayer, M. T.; Gratzel, M. Efficient photosynthesis of carbon monoxide from CO_2 using perovskite photovoltaics. *Nat. Commun.* **2015**, *6*, 7326.

(3) Jeon, H. S.; Koh, J. H.; Park, S. J.; Jee, M. S.; Ko, D. H.; Hwang, Y. J.; Min, B. K. A monolithic and standalone solar-fuel device having comparable efficiency to photosynthesis in nature. *J. Mater. Chem. A* **2015**, *3*, 5835−5842.

(4) Kumar, B.; Llorente, M.; Froehlich, J.; Dang, T.; Sathrum, A.; Kubiak, C. P. Photochemical and photoelectrochemical reduction of CO_2. *Annu. Rev. Phys. Chem.* **2012**, *63*, 541.

(5) Jones, J. P.; Prakash, G. K. S.; Olah, G. A. Electrochemical CO_2 reduction: recent advances and current trends. *Isr. J. Chem.* **2014**, *54*, 1451−1466.

(6) Hori, Y. Electrochemical CO_2 reduction on metal electrodes. *Modern Aspects of Electrochemistry* **2008**, *42*, 89−189.

(7) Chen, Y. H.; Li, C. W.; Kanan, M. W. Aqueous CO_2 reduction at very low overpotential on oxide-derived Au nanoparticles. *J. Am. Chem. Soc.* **2012**, *134*, 19969−19972.

(8) Kuhl, K. P.; Cave, E. R.; Abram, D. N.; Jaramillo, T. F. New insights into the electrochemical reduction of carbon dioxide on metallic copper surfaces. *Energy Environ. Sci.* **2012**, *5*, 7050−7059.

(9) Li, C. W.; Kanan, M. W. CO_2 Reduction at low overpotential on Cu electrodes resulting from the reduction of thick Cu2O films. *J. Am. Chem. Soc.* **2012**, *134*, 7231−7234.

(10) Hirota, K.; Tryk, D. A.; Yamamoto, T.; Hashimoto, K.; Okawa, M.; Fujishima, A. Photoelectrochemical reduction of CO_2 in a high-pressure CO_2 plus methanol medium at p-type semiconductor electrodes. *J. Phys. Chem. B* **1998**, *102*, 9834−9843.

(11) Frese, K. W.; Canfield, D. Reduction of CO_2 on n-GaAs electrodes and selective methanol synthesis. *J. Electrochem. Soc.* **1984**, *131*, 2518−2522.

(12) Aurianblajeni, B.; Halmann, M.; Manassen, J. Electrochemical measurements on the photo-electrochemical reduction of aqueous carbon-dioxide on para-gallium phosphide and para-gallium arsenide semiconductor electrodes. *Sol. Energy Mater.* **1983**, *8*, 425−440.

(13) Ikeda, S.; Yamamoto, A.; Noda, H.; Maeda, M.; Ito, K. Influence of surface-treatment of the p-Gap photocathode on the photo-electrochemical reduction of carbon-dioxide. *Bull. Chem. Soc. Jpn.* **1993**, *66*, 2473−2477.

(14) Noda, H.; Yamamoto, A.; Ikeda, S.; Maeda, M.; Ito, K. Influence of light-intensity on photoelectroreduction of CO_2 at a p-Gap photocathode. *Chem. Lett.* **1990**, 1757−1760.

(15) Yoneyama, H.; Sugimura, K.; Kuwabata, S. Effects of electrolytes on the photoelectrochemical reduction of carbon-Dioxide at illuminated para-type cadmium telluride and para-type indium-phosphide electrodes in aqueous-solutions. *J. Electroanal. Chem. Interfacial Electrochem.* **1988**, *249*, 143−153.

(16) Chen, Y. K.; Xiang, C. X.; Hu, S.; Lewis, N. S. Modeling the performance of an integrated photoelectrolysis system with 10 x solar concentrators. *J. Electrochem. Soc.* **2014**, *161*, F1101−F1110.

(17) Haussener, S.; Hu, S.; Xiang, C. X.; Weber, A. Z.; Lewis, N. S. Simulations of the irradiation and temperature dependence of the efficiency of tandem photoelectrochemical water-splitting systems. *Energy Environ. Sci.* **2013**, *6*, 3605−3618.

(18) Haussener, S.; Xiang, C. X.; Spurgeon, J. M.; Ardo, S.; Lewis, N. S.; Weber, A. Z. Modeling, simulation, and design criteria for photoelectrochemical water-splitting systems. *Energy Environ. Sci.* **2012**, *5*, 9922−9935.

(19) Xiang, C.; Chen, Y.; Lewis, N. S. Modeling an integrated photoelectrolysis system sustained by water vapor. *Energy Environ. Sci.* **2013**, *6*, 3713−3721.

(20) Hatsukade, T.; Kuhl, K. P.; Cave, E. R.; Abram, D. N.; Jaramillo, T. F. Insights into the electrocatalytic reduction of CO_2 on metallic silver surfaces. *Phys. Chem. Chem. Phys.* **2014**, *16*, 13814−13819.

(21) Sun, K.; Saadi, F. H.; Lichterman, M. F.; Hale, W. G.; Wang, H. P.; Zhou, X. H.; Plymale, N. T.; Omelchenko, S. T.; He, J. H.; Papadantonakis, K. M.; Brunschwig, B. S.; Lewis, N. S. Stable solar-driven oxidation of water by semiconducting photoanodes protected by transparent catalytic nickel oxide films. *Proc. Natl. Acad. Sci. U. S. A.* **2015**, *112*, 3612−3617.

(22) Jin, J.; Walczak, K.; Singh, M. R.; Karp, C.; Lewis, N. S.; Xiang, C. An experimental and modeling/simulation-based evaluation of the efficiency and operational performance characteristics of an integrated,

DOI: 10.1021/acsenergylett.6b00134
ACS Energy Lett. 2016, 1, 273−280

membrane-free, neutral pH solar-driven water-splitting system. *Energy Environ. Sci.* **2014**, *7*, 3371−3380.
(23) Singh, M. R.; Papadantonakis, K.; Xiang, C. X.; Lewis, N. S. An electrochemical engineering assessment of the operational conditions and constraints for solar-driven water-splitting systems at near-neutral pH. *Energy Environ. Sci.* **2015**, *8*, 2760−2767.
(24) Johnson, K. S. Carbon-dioxide hydration and dehydration kinetics in sea-water. *Limnol. Oceanogr.* **1982**, *27*, 849−855.
(25) Schulz, K. G.; Riebesell, U.; Rost, B.; Thoms, S.; Zeebe, R. E. Determination of the rate constants for the carbon dioxide to bicarbonate inter-conversion in pH-buffered seawater systems. *Mar. Chem.* **2006**, *100*, 53−65.
(26) *CRC Handbook of Chemistry and Physics*, 96th ed.; CRC Press: Boca Raton, FL, 2015.

DOI: 10.1021/acsenergylett.6b00134
ACS Energy Lett. 2016, 1, 273−280